

# Accurate determination of local defocus and specimen tilt in electron microscopy

Joseph A. Mindell<sup>a</sup> and Nikolaus Grigorieff<sup>b,\*</sup>

<sup>a</sup> *Membrane Transport Biophysics Unit, National Institute of Neurological Disease and Stroke, National Institutes of Health, 36 Convent Drive, MSC4066, Bethesda, MD 20892-4066, USA*

<sup>b</sup> *Howard Hughes Medical Institute, Rosenstiel Basic Medical Sciences Research Center, MS029, Brandeis University, 415 South Street, Waltham, MA 02454-9110, USA*

Received 2 December 2002, and in revised form 25 March 2003

## Abstract

Accurate knowledge of defocus and tilt parameters is essential for the determination of three-dimensional protein structures at high resolution using electron microscopy. We present two computer programs, CTFFIND3 and CTFTILT, which determine defocus parameters from images of untilted specimens, as well as defocus and tilt parameters from images of tilted specimens, respectively. Both programs use a simple algorithm that fits the amplitude modulations visible in a power spectrum with a calculated contrast transfer function (CTF). The background present in the power spectrum is calculated using a low-pass filter. The background is then subtracted from the original power spectrum, allowing the fitting of only the oscillatory component of the CTF. CTFTILT determines specimen tilt parameters by measuring the defocus at a series of locations on the image while constraining them to a single plane. We tested the algorithm on images of two-dimensional crystals by comparing the results with those obtained using crystallographic methods. The images also contained contrast from carbon support film that added to the visibility of the CTF oscillations. The tests suggest that the fitting procedure is able to determine the image defocus with an error of about 10 nm, whereas tilt axis and tilt angle are determined with an error of about 2° and 1°, respectively. Further tests were performed on images of single protein particles embedded in ice that were recorded from untilted or slightly tilted specimens. The visibility of the CTF oscillations from these images was reduced due to the lack of a carbon support film. Nevertheless, the test results suggest that the fitting procedure is able to determine image defocus and tilt angle with errors of about 100 nm and 6°, respectively.

© 2003 Elsevier Science (USA). All rights reserved.

*Keywords:* Electron microscopy; Contrast transfer function; Algorithm; Tilt determination

## 1. Introduction

Electron cryo-microscopy is a versatile technique to determine the three-dimensional (3D) structure of proteins and protein complexes. It can be applied to samples of different symmetry and geometry, such as two-dimensional (2D) crystals (Henderson et al., 1990; Kühlbrandt and Wang, 1991; Mindell et al., 2001; Murata et al., 2000; Nogales et al., 1998), helical particles (Morgan et al., 1995; Wells et al., 1999; Wendt et al., 2002), highly symmetrical viruses (Böttcher et al., 1997; Kuhn et al., 2002; Zhou et al., 2001), and other particles with lower or no

symmetry (Frank and Agrawal, 2000; Grigorieff, 1998; Ranson et al., 2001). The processing of an image obtained from any of these samples usually includes the determination of lens defocus and astigmatism needed to correct the measured data for the contrast transfer function (CTF) of the electron microscope (Erickson and Klug, 1971; Wade, 1992). The correction is necessary because the CTF causes resolution-dependent amplitude modulations (Thon rings; Thon, 1966) and phase reversals in the image (Fig. 1). The Thon rings can be observed in a power spectrum of an image, and they are particularly strong when the image contains additional contrast from a carbon film supporting the sample. Towards higher resolution, as the CTF oscillations become more rapid, accurate knowledge of defocus and astigmatism are essential for correct determination of the image phases.

\* Corresponding author. Fax: +781-736-2419.

E-mail address: [niko@brandeis.edu](mailto:niko@brandeis.edu) (N. Grigorieff).

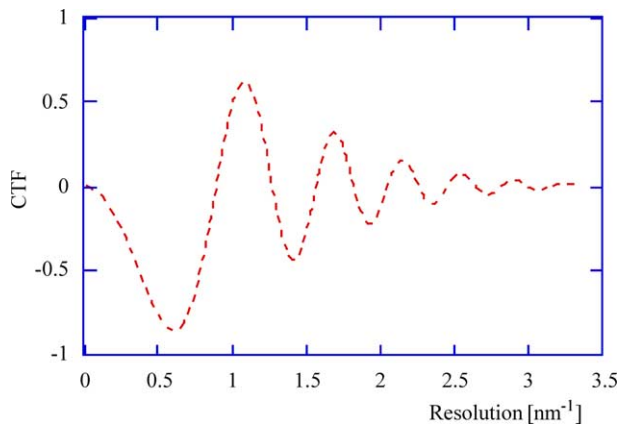


Fig. 1. Contrast transfer function and envelope. The CTF of an electron microscope produces periodic phase reversals and has an amplitude which is attenuated towards higher resolution by an approximately Gaussian envelope function. For this plot, an electron beam voltage of 200 kV, a spherical aberration coefficient of  $C_s = 2.0$  mm, and a defocus of 500 nm was assumed. The envelope was calculated using an exponential function,  $\exp(-g^2/g_{\text{eff}}^2)$ , where  $g$  is the magnitude of the scattering vector and  $g_{\text{eff}}$  describes the effective width of the envelope function. Here, a value of  $1.6 \text{ nm}^{-1}$  was used for  $g_{\text{eff}}$ .

When ordered samples are imaged, such as 2D crystals, the diffraction patterns calculated from the images can be used to determine image defocus and astigmatism accurately (for example, see Henderson et al., 1986). Yet, methods based on diffraction patterns are not applicable to samples that contain aperiodic structures, such as single protein molecules and complexes. In those cases, image defocus and astigmatism can still be determined from the shape and position of the Thon rings. Often, samples of single protein molecules are prepared for electron microscopy using a carbon film containing approximately  $1 \mu\text{m}$  wide holes. This has the advantage that images of molecules suspended in a thin layer of ice inside the holes show reduced background due to the absence of the carbon support film. However, the lack of contrast from a carbon film also means that the Thon rings are reduced in their visibility, making the determination of defocus parameters more difficult. An additional complication arises with tilted specimens because the amount of defocus is then also a function of the position on the specimen. Tilt can be introduced deliberately to obtain 3D information of a sample that exhibits a preferred orientation on the carbon support film, such as a 2D crystal. Often, however, a small but significant tilt is introduced unintentionally due to undulations in the carbon support film. These undulations can sometimes be enhanced when the specimen is frozen, due to the difference in thermal expansion coefficients between the carbon support film and the metal grid the film is deposited on. This effect is sometimes referred to as ‘cryo-crikling’ and can be reduced by using molybdenum grids (Vonck, 2000).

Image formation in the electron microscope results from a combination of sample-induced elastic and in-

elastic electron scattering. In general, inelastic scattering produces an almost featureless background in the image power spectrum that is high at low resolution and falls off towards higher resolution (Zhu et al., 1997). Amplitude contrast in an image is produced by high-angle scattering when the electrons are scattered outside the objective aperture. The elastically scattered electrons that pass through the objective aperture produce the phase contrast that contains most of the structural information in cryo-EM of unstained specimens; the amount of amplitude contrast from these specimens is usually very small. The amplitude and phase contrast are modulated by the CTF of the microscope which is a function of defocus, astigmatism, lens errors, electron wave length, as well as temporal and spatial coherence of the electron beam (Zhu et al., 1997). The image recording process on film or CCD also contributes to the CTF (Koeck, 2000). The inelastic component of the contrast in an image giving rise to the smooth background is not used in current structural analyses.

Precise determination of the CTF based solely of the shape and position of Thon rings is difficult; it would require knowledge of all the parameters listed above as well as a detailed understanding of inelastic and multiple scattering. Comprehensive determination of the CTF from images of single molecules has been successful with energy-filtered images, where the bulk of the background due to inelastic scattering was removed (Zhu et al., 1997). Energy filters are not, however, routinely available on electron microscopes used in structural biology. Even without a detailed understanding of all the scattering components contributing to the contrast in an unfiltered image, the oscillations due to the CTF can usually be interpreted in a straight-forward manner. The periodic phase reversals corresponding to these oscillations are the only effect of the CTF on image phases, and these in turn are the predominant determinants of molecular structure (Ramachandran and Srinivasan, 1961). The phase reversals can be roughly described by a simple oscillating function of constant amplitude, determined by defocus, astigmatism, and spherical aberration of the objective lens. In the comprehensive description, this in turn is multiplied by an envelope function which monotonically attenuates the CTF towards higher spatial resolution, and which captures the effects of spatial and temporal beam incoherence (Fig. 1; Wade, 1992). We show here that defocus and astigmatism, the parameters which determine the oscillatory component of the CTF, can be determined in images of untilted specimens with sufficient accuracy to obtain corrected phases at 0.3-nm resolution without knowing the shape of the envelope. The procedure of defocus determination for images of untilted specimens has been implemented in a computer program called CTF-FIND3. We further show that the defocus information across an image of a tilted specimen can be used to

accurately determine specimen tilt axis and tilt angle. The entire process of defocus and tilt determination has been automated in a new computer program called CTFTILT. Both programs are written in FORTRAN 77 code and are available from the corresponding author. The programs were tested on a 2.4-GHz Pentium 4 PC running Linux. For moderately sized images of about  $6000 \times 6000$  pixels, the analysis performed by CTF-FIND3 is completed in about 2 min, whereas the analysis performed by CTFTILT is completed about 15 min.

## 2. Methods

### 2.1. Determination of defocus from power spectra

To determine the defocus and astigmatism for an image, our objective is to fit the oscillatory component of the measured power spectrum in two dimensions. However, to do so on a full sized image ( $>10,000 \times 10,000$  pixels) would be computationally expensive. Furthermore, such a fit would be contaminated by portions of the image containing unexposed areas of film or other aberrations. Thus, we subdivide the image into small square tiles, then calculate the power spectrum of each tile, summing the individual spectra to form a final working power spectrum. This approach of estimating the power spectrum of an image was also used by Fernandez et al. (1997) and Zhu et al. (1997). In addition to reducing the time for subsequent computational steps, this operation allows us to discard irregular areas based on their pixel density variance. For example, tiles showing the edge of the electron beam or contaminating ice will have a significantly higher variance than the average image variance, whereas tiles containing an unexposed area of the negative would have a much smaller variance: such areas are excluded from the final averaged power spectrum. It is important, however, to ensure that the size of the tiles is sufficiently large such that the CTF oscillations in the power spectra are clearly resolved in the resolution range of interest.

The accurate determination of defocus requires separation of the oscillatory component of the power spectrum from the smooth background originating from inelastic scattering (Zhu et al., 1997). Background subtraction from the power spectrum of an image is an essential first step for the CTF fitting procedure because the background usually has an overwhelming magnitude compared to the CTF oscillations visible in the spectrum. It is, therefore, part of most CTF fitting algorithms. For example, the background was determined in radially averaged power spectra by fitting a smooth function (for example, a Gaussian) to the observed minima in the spectrum (Conway and Steven, 1999; Zhou and Chiu, 1993; Zhu and Frank, 1994; Zhu et al., 1997). The radial averaging meant that any astigmatism

present in the image was ignored. In another approach, the smooth component of an image power spectrum was determined by fitting a cubic spline function to the radially averaged spectrum (Tani et al., 1996). Unlike in the previous case, the subtraction of a smooth cubic spline leads to negative values for the CTF minima. To take astigmatism into account, Tani et al. (1996) divided the two-dimensional power spectrum into angular zones of approximately constant defocus and analyzed the radial average over every zone separately. van Heel et al. (2000) measured the astigmatism in an image by performing a full 2D fit to the power spectrum, an approach we will also adopt here.

In this paper, we make no attempt to rigorously determine the contributions of inelastic scattering, incoherence, etc. to the background: rather, we empirically estimate the background as the monotonically decreasing component of the power spectrum. This could be determined in a number of ways, for example, using a cubic spline fit (Tani et al., 1996), or by calculating a low-pass filtered version of the spectrum (van Heel et al., 2000). We chose to smooth the power spectrum using a box convolution. This approach yields the best estimate of a linear background underlying oscillations of constant amplitude. However, the slope of the background observed in our power spectra varies significantly—it is steeper at low resolution than at high resolution. Therefore, we estimate the smooth background  $P_{\text{smooth}}$  from the square root of the averaged power spectrum which reduces the change in the slope:

$$P_{\text{smooth}}(i, j) = \left[ \sum_{l, m = -N_{\text{box}}/2}^{N_{\text{box}}/2} \sqrt{P_{\text{ave}}(i + l, j + m)} \right]^2, \quad (1)$$

where  $N_{\text{box}}$  is the size of the box and  $P_{\text{ave}}$  is the averaged power spectrum. The smoothed image is then subtracted from the power spectrum of the original image, producing a corrected spectrum,  $P_{\text{corr}}$ , suitable for further CTF analysis (Fig. 2b):

$$P_{\text{corr}}(i, j) = P_{\text{ave}}(i, j) - P_{\text{smooth}}(i, j). \quad (2)$$

To determine defocus and astigmatism, a two-dimensional CTF has to be fitted:

$$\text{CTF}(\lambda, \mathbf{g}, \Delta f, C_s) = -w_1 \sin[\chi(\lambda, \mathbf{g}, \Delta f, C_s)] - w_2 \cos[\chi(\lambda, \mathbf{g}, \Delta f, C_s)], \quad (3)$$

with

$$\chi(\lambda, \mathbf{g}, \Delta f, C_s) = \pi \lambda g^2 (\Delta f - 1/2 \lambda^2 g^2 C_s), \quad (4)$$

and the two constants  $w_1$  and  $w_2$  are given by the percentage of amplitude contrast,  $A$ , in the image:

$$\begin{aligned} w_1 &= \sqrt{1 - A^2}, \\ w_2 &= A. \end{aligned} \quad (5)$$

Usually, the value for  $A$  ranges from 0.07 (Toyoshima and Unwin, 1988; Toyoshima et al., 1993) to 0.14 (Smith

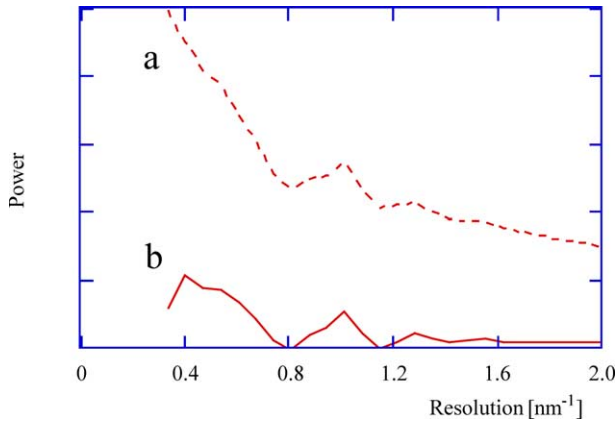


Fig. 2. Background subtraction (a) shows a plot of a radial average of the power spectrum obtained for image b3730 (see Table 1). Before fitting defocus values, the smooth background has to be subtracted. The radial average of the background-subtracted power spectrum is shown in (b).

and Langmore, 1992) for proteins embedded in ice and 0.19 (Zhu and Frank, 1994) to 0.35 (Erickson and Klug, 1971) for proteins embedded in stain (uranyl acetate).  $\lambda$  is the electron wavelength,  $\mathbf{g}$  is the scattering vector describing the difference between the wave vectors  $\mathbf{k}$  and  $\mathbf{k}'$  of the unscattered and scattered electrons,  $\mathbf{g} = \mathbf{k}' - \mathbf{k}$ , and  $C_s$  is the spherical aberration coefficient of the objective lens. The defocus  $\Delta f$  is given by (Henderson et al., 1986)

$$\Delta f = 1/2 [DF_1 + DF_2 + (DF_1 - DF_2) \cos(2[\alpha_g - \alpha_{ast}])], \quad (6)$$

where  $DF_1$  and  $DF_2$  are the two defocus values describing the defocus in two perpendicular directions in an image when astigmatism is present,  $\alpha_{ast}$  gives the angle between the first direction (described by  $DF_1$ ) and the  $X$ -axis, and  $\alpha_g$  is the angle between the direction of the scattering vector  $\mathbf{g}$  and the  $X$ -axis. Note that in Eq. (3) a positive value for the defocus indicates an underfocus. The definitions of the parameters in Eq. (6) are summarized in Fig. 3.

The defocus parameters can be determined by a least-squares fit between the positions of the minima in the calculated squared CTF and the observed power spectra (Conway and Steven, 1999; Zhu et al., 1997). This approach relies on the radial averaging of the power spectrum to reliably detect the positions of the minima. The defocus parameters can also be determined by a least-squares fit between the calculated CTF and square root of the observed power spectrum (Frank, 1972) or between the square of the calculated CTF and the power spectrum (Henderson et al., 1986). This requires the additional determination of a scaling factor. We use an approach similar to that adopted by Tani et al. (1996) and van Heel et al. (2000) and fit the CTF by maximizing the correlation coefficient

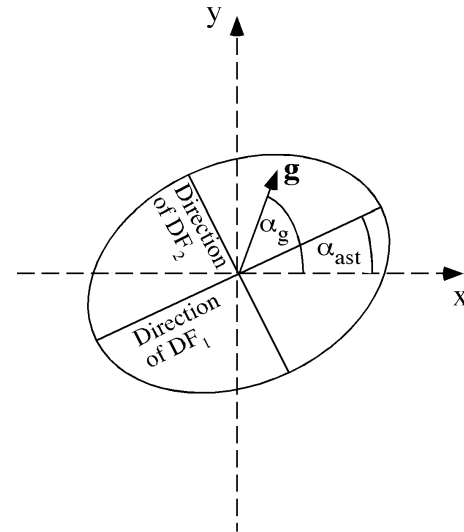


Fig. 3. Definitions for the CTF parameters  $DF_1$ ,  $DF_2$ , and  $\alpha_{ast}$ . The angle  $\alpha_g$  of the scattering vector  $\mathbf{g} = \mathbf{k}' - \mathbf{k}$  ( $\mathbf{k}$ , wave vector of the incident wave;  $\mathbf{k}'$ , wave vector of the scattered wave) is used in Eq. (6), indicating the point where the CTF is evaluated.

$$CC_p(DF_1, DF_2, \alpha_{ast}) = \left\{ \sum_{i,j} P_{corr}(i,j) * CTF^2(\lambda, \mathbf{g}(i,j), \Delta f(i,j), C_s) \right\} / \left\{ \sqrt{\sum_{i,j} P_{corr}^2(i,j) \sum_{i,j} CTF^4(\lambda, \mathbf{g}(i,j), \Delta f(i,j), C_s)} \right\}. \quad (7)$$

Here, the scattering vector  $\mathbf{g}$  and defocus  $\Delta f$  have been written as explicit functions of the pixel coordinates  $i, j$  in the power spectrum. The maximum correlation is found by performing a grid search of defocus values  $DF_1$  and  $DF_2$ , and astigmatic angle  $\alpha_{ast}$ , followed by a function maximization using the conjugate gradient method. The fitting procedure has been implemented in a computer program called CTFFIND3 which determines CTF parameters for images from untilted specimens.

## 2.2. Determination of specimen tilt axes and angle

The defocus parameters are essentially a measure of the distance between the sample and the focal plane of the objective lens. Therefore, tilt information can be obtained from the defocus variation across the image. The procedure to determine defocus parameters averaged over the entire image, as discussed in the previous section, can also be applied to a small area of the image to find local defocus parameters. In contrast to the previous case, the power spectra calculated from smaller areas of the image will be much noisier, and an accurate determination of local defocus parameters based on

such power spectra will be difficult. To avoid this problem, we assume that the sample is flat within the illuminated area. The assumption agrees with recently published results by van Heel et al. (2000) who also carried out defocus measurements in an image of a tilted specimen. The fitting of all background-subtracted power spectra, calculated locally for each tile, can then be done simultaneously, and the defocus variation from tile to tile can be constrained to a single plane. This is a computationally rather expensive task since a typical high-resolution scan of an image will yield about  $10,000 \times 10,000$  pixels, and about 6000 tiles. It would be time-consuming to exhaustively explore the entire parameter space to find the global correlation maximum. Rather we seek to narrow the parameter space by determining approximate values for several of the variables of interest before attempting a more rigorous CTF fit.

A flow chart of the algorithm for the computer program CTFTILT is shown in Fig. 4. We begin by determining an approximate direction for the tilt axis. The tilt axis can be defined as the direction of a line with constant height (defocus),  $z$ . In an ideal image, a series of tiles along such a line would have identical power spectra, whereas the spectra of tiles along a line in any other direction would vary due to the change in defocus. In a real image, the tilt axis should be the direction of minimum variance between tiles. Our empirical analysis has determined that the signal from a single line of tiles is insufficient to determine the tilt axis: to increase the signal we use the tiles from eleven adjacent parallel lines for variance minimization. When the number of lines is increased further, the visibility of the Thon rings in the average power spectrum calculated from tiles along the lines (see below) is reduced significantly in images of highly tilted specimens. In our implementation, the power spectra of a series of tiles along eleven parallel lines (at angle  $\phi$  to the  $X$ -axis) are calculated (Fig. 5), and the variance between them is evaluated:

$$\text{VAR}_\phi = \frac{1}{N} \sum_{k=1}^N \sum_{i,j} [P_{\text{tile}}^k(i,j) - P_{\text{ave}}(i,j)]^2. \quad (8)$$

The approximate direction of the tilt axis can be found by minimizing  $\text{VAR}_\phi$  on the interval  $(0, 180^\circ)$  using a simple search. A search increment of  $2^\circ$  is sufficient in practice. For certain directions of the lines, the tile corners overlap, leading to a reduction of variance between the power spectra which obscures the defocus-related variation. To eliminate this effect, we exclude any signal from the corners of the tiles by masking the tiles with a circular mask (Fig. 5). Once the tilt axis is approximately known, the background-subtracted average of the power spectra along the eleven lines are used to determine defocus and astigmatism, as discussed in the previous section.

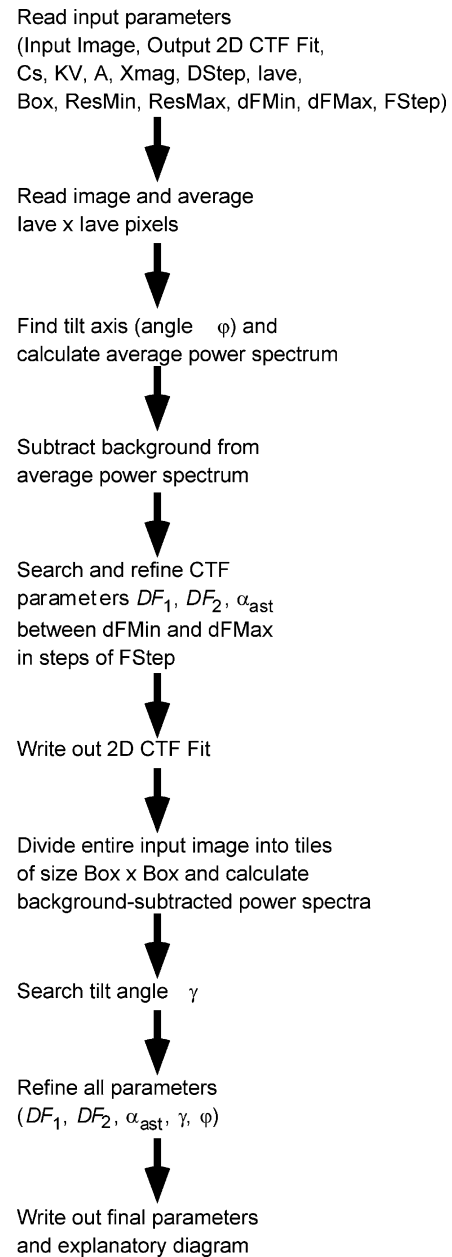


Fig. 4. Flow chart for the algorithm implemented in CTFTILT. The input image can be of any dimension. For easy comparison, an output image is generated showing on one side the background-subtracted power spectrum, and on the other side the fitted CTF.  $C_s$  and  $K_V$  are the spherical aberration coefficient of the objective lens in millimeter, and the electron beam voltage in kilovolts, respectively.  $A$  is the expected amount of amplitude contrast. This value does not need to be accurate as the fitting procedure is not very sensitive to small changes in  $A$ .  $X_{\text{mag}}$  is the magnification of the image and  $D_{\text{Step}}$  is the pixel resolution of the detector converting the image into a digital array.  $I_{\text{ave}}$  is an integer to indicate a compression factor used to reduce the size of the image for increased computational speed once the image has been read in.  $I_{\text{ave}} = 1$  means no compression.  $Box$  gives the size of the tiles used to subdivide the image.  $Res_{\text{Min}}$  and  $Res_{\text{Max}}$  indicate the resolution range for the CTF fit.  $dF_{\text{Min}}$  and  $dF_{\text{Max}}$  give lower and upper limits for the initial CTF parameter search which is done with step size  $F_{\text{Step}}$ .

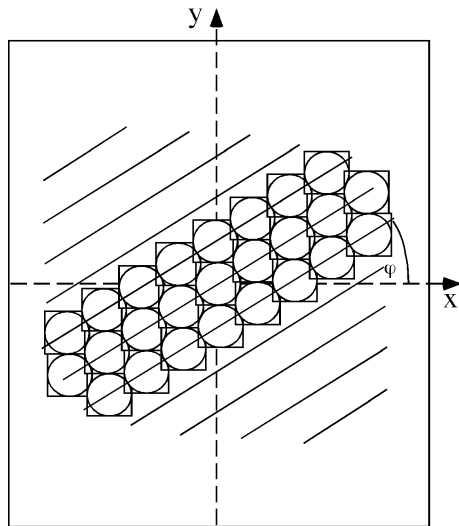


Fig. 5. Determination of tilt axis. Power spectra are calculated for each tile along the eleven parallel lines (tiles are only indicated for the three central lines). The angle  $\varphi$  is searched in  $2^\circ$  steps to find the direction in which the variance between the power spectra is minimized.

The last parameter to be determined is the tilt angle. An approximate value is found again by performing a search. However, the fitting procedure is now extended across the entire image to include all tiles. If we assume that the entire imaged area lies in a single plane, we can write for the defocus  $\Delta f$  at a point  $x, y$  on the image

$$\Delta f = \Delta f_0 + [(x - x_0) \sin(\varphi) - (y - y_0) \cos(\varphi)] \tan(\gamma). \quad (9)$$

Here,  $x_0, y_0$  is the center of the image where the defocus  $\Delta f_0$  and astigmatism values were determined in the previous step.  $\varphi$  is the angle between the tilt axis and the  $X$ -axis and  $\gamma$  is the tilt angle. The search is performed in the interval  $[-65^\circ, +65^\circ]$ , and a step size of  $10^\circ$  was found to be sufficient in practice to find the correct tilt angle. The final step consists of a refinement of all five parameters ( $DF_1, DF_2, \alpha_{ast}, \gamma$ , and  $\varphi$ ) using conjugate gradient maximization of the correlation between calculated CTF and observed, background-subtracted power spectra.

### 3. Results

Because the CTF is a complex function of many variables, we have used a largely empirical approach to extract the defocus and tilt parameters which strongly influence the final image phases. The two major features of the algorithm for untilted images are the background subtraction and the full, two-dimensional fit of the power spectrum to an unattenuated CTF.

The fitting algorithm implemented in CTFFIND3 was tested on high-resolution electron micrographs of 2D crystals used to calculate a 0.26-nm resolution pro-

jection structure of bacteriorhodopsin (Grigorieff et al., 1995). The samples were prepared using a continuous carbon support film, and the crystals were frozen-hydrated in ice. These images are ideal test objects since the defocus parameters were refined crystallographically to high resolution and, therefore, should represent very close approximations to the true defocus settings. The images were recorded at a nominal magnification of 60,000, using the liquid helium field emission electron microscope SOFIE (Zemlin et al. (1996),  $C_s = 2.0$  mm, acceleration voltage = 200 kV). All four images in the data set contained  $6000 \times 6000$  pixels and the following parameters were used (see input box in Fig. 4): Amplitude contrast ( $A$ ) = 7%, scanner pixel resolution (DStep) =  $7.5 \mu\text{m}$ , pixel averaging (Iave) = 1, tile size (Box) = 128 pixels, resolution range (ResMin, ResMax) = 20–0.3 nm, defocus search range (dFMin, dFMax, FStep) = 100–1000 nm in 50-nm steps. The raw and the background-subtracted power spectra for image b3730 are shown in Fig. 2 which provides a preliminary validation of our background subtraction: The minima of the background-subtracted spectrum are negative but close to zero, and the trace falls off to zero at high resolution. The small deviation of the minima from zero may at first appear surprising since the background subtraction is merely a subtraction of a low-pass filtered image of the original power spectrum. One would therefore expect the minima in the background-subtracted spectrum to be more negative than observed in Fig. 2. However, the background estimated by the box convolution in Eq. (1) is smaller than the local average of the power spectrum for two reasons: First, the background in the power spectrum has a slope that is negative and becomes smaller in magnitude towards higher resolution. This leads to an underestimate of the background by the box convolution. Second, the box convolution is performed on the square root of the power spectrum, and the resulting smooth background is subsequently squared (Eq. (1)), again giving an underestimate of the average local power in the spectrum.

The results of the fits are summarized in Table 1 and show that the defocus values were determined to be within 10 nm, and the astigmatic angle was measured within  $5^\circ$  of the crystallographic values. Fig. 6a shows a montage of the fitted two-dimensional squared CTF and the observed, background-subtracted power spectrum of image b3730. There is good agreement between the two halves of the montage. Fig. 6b shows line plots of the background-subtracted power spectrum and the fitted squared CTF. Though the curves appear quite different, the zeros of the observed spectrum correspond closely to those of the fit. Since these are the locations of the phase reversals, we appear to have determined enough about the CTF to understand its phase behavior. Close inspection of Fig. 6b suggests, however, that there is some discrepancy between the locations of the CTF zeros

Table 1  
Comparison of defocus values from bacteriorhodopsin images

Image	DF <sub>1</sub> (nm)			DF <sub>2</sub> (nm)			α <sub>ast</sub> (deg)			CC <sub>p</sub>
	Crys.	CTFFIND	Δ <sub>1</sub>	Crys.	CTFFIND	Δ <sub>2</sub>	Crys.	CTFFIND	Δ <sub>z</sub>	CTFFIND
b3730	601.0	597.5	-3.5	531.4	525.1	-6.3	8.6	4.3	4.3	0.17
b3736	472.0	473.3	1.3	545.8	555.9	10.1	103.1	99.9	3.2	0.18
b3737	572.2	577.4	5.2	490.4	491.8	1.4	11.9	11.2	0.7	0.18
b3739	400.7	398.1	-2.6	316.8	317.1	0.3	5.5	6.5	1.0	0.23

Crystallographic defocus values including astigmatism (DF<sub>1</sub>, DF<sub>2</sub>, and α<sub>ast</sub>) were determined by minimizing phase residuals between individual images and a merged data set used to calculate a projection map of bacteriorhodopsin at 0.26-nm resolution (ref).

Δ<sub>1</sub>, Δ<sub>2</sub> and Δ<sub>z</sub> are the differences between crystallographic values and values obtained using CTFFIND3.

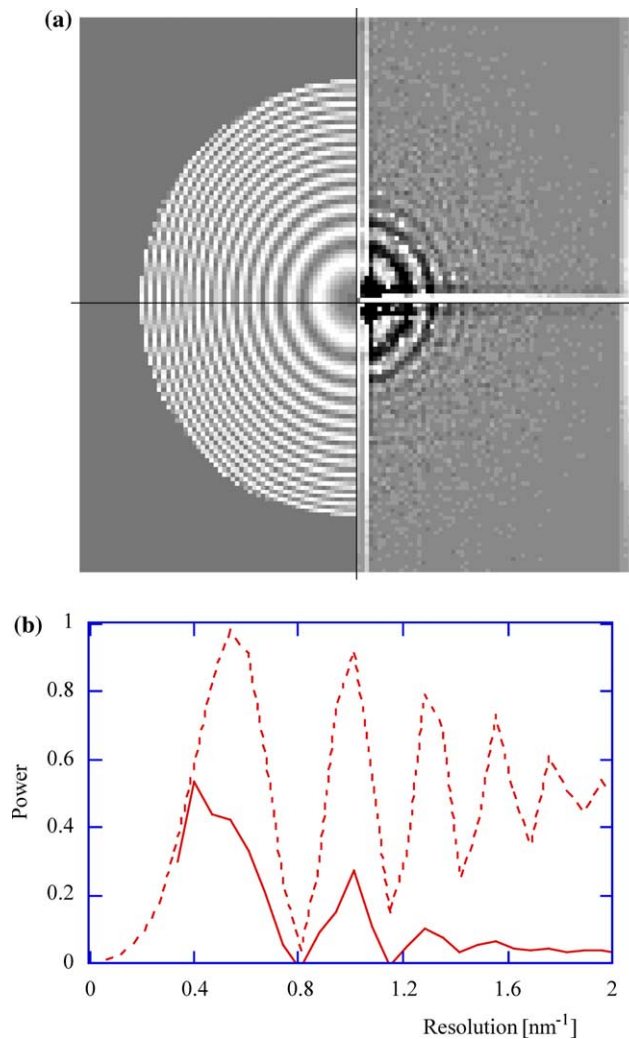


Fig. 6. CTF fit (a) The diagnostic output image for image b3730, showing the average background-subtracted power spectrum on the right, and the fitted CTF on the left. The two defocus parameters, DF<sub>1</sub> and DF<sub>2</sub>, and the astigmatic angle α<sub>ast</sub>, were determined to be 597.5 nm, 525.1 nm, and 4.3°, respectively (see Table 1). Crystal reflections originating from the 2D crystal in the image are visible in the power spectrum on the right. However, they are not noticeable in the radial average. (b) Plot of the radial average of the average background-subtracted power spectrum in (a) (solid line) and the fitted CTF (dotted line). The radial averaging leads to a small reduction in amplitude of the fitted CTF towards higher resolution since there is a small astigmatism present in the image.

beyond a resolution of about 1.8 nm<sup>-1</sup>. The apparent discrepancy may be due to an inaccurate value used for the amplitude contrast (*A*), or a lack in the sampling resolution of the spectrum and fit. An inaccurate value for the amplitude contrast may indeed lead to errors in the fit, as discussed below. However, the results presented in Table 1 show that for the parameters used in all four fits the errors are small. To estimate the effect of the errors in an untilted image, the CTF is plotted in Fig. 7 using an average of the two defocus values from the fit in Fig. 6. Fig. 7 also shows CTF plots for defocus values 10 nm higher and lower than the average defocus. These additional plots illustrate how much the CTF changes at a resolution of 0.3 nm when the defocus value has an error of 10 nm, demonstrating that an error of 10-nm shifts the CTF zero at 0.3-nm resolution by about one-tenth of a period. As a result, some of the image data, when corrected for their CTF, would acquire the wrong phase. However, the affected data are close to zeros of the CTF; thus, these data will generally be weak and have poor signal-to-noise ratios. Such data will contribute minimally to a final reconstruction since they

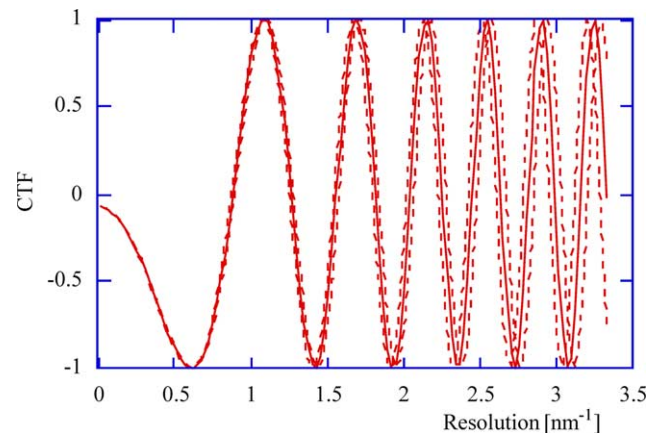


Fig. 7. Error in the measured defocus value. The CTF is plotted for different defocus values. The solid line shows the CTF for an underfocus of 500 nm, and the two dotted lines show CTF plots for 490 and 510 nm underfocus. Seven percent amplitude contrast was included in these plots, and a microscope running at 200 kV and a spherical aberration coefficient of 2 mm were assumed.

will be averaged with stronger data from other images. The phases for most of the data, especially for data at points where the CTF assumes large values, are measured correctly, and can be used to derive structural information at 0.3-nm resolution.

Table 2 presents results from a number of additional CTF fits for the 2D crystals of bacteriorhodopsin using different input parameters to test the robustness of the algorithm. We varied the following parameters, one at a time: amplitude contrast (*A*), tile size (*Box*), and the high-resolution limit (*ResMax*). Whenever the fitted values for defocus and astigmatic angle agreed with the corresponding values in Table 1 within 10 nm and 5°, respectively, a dot (·) is shown. When the fits produced values outside these limits, the changes are explicitly shown. Of the various values used for the amplitude contrast, only a value of 35% produced changes in the defocus values larger than 10 nm. However, the changes were all negative and of approximately the same magnitude, about –12 nm. An increased amplitude contrast shifts the zeros of the fitted CTF towards lower resolution. To compensate for this shift, the defocus values producing the best fit are lower than what is obtained with smaller values for the amplitude contrast. This leads to the observed systematic shift towards smaller defocus values. Of the different tile sizes tested, only the 50 × 50 pixel tile size lead to a failure in the algorithm. The failure is due to the reduced sampling resolution of the power spectra. Of the resolution limits tested, the algorithm failed when the resolution of the fit was restricted to data below 1 nm (or lower). This is not surprising since the first two CTF zeros of the power spectra are at about 1.2 and 0.85 nm, leaving only one CTF zero (or no CTF zero) within the fitted range.

As a second test of CTFFIND3, the defocus and astigmatism was determined for 268 images of single mitochondrial complex I molecules. Some of these im-

ages were used to determine the 3D structure of complex I at 2.2-nm resolution (Grigorieff, 1998). These images are qualitatively different from those of the 2D crystals of bacteriorhodopsin because they were collected from areas of the sample that did not contain much carbon. Therefore, the only contrast visible in those images arose from the ice and the protein embedded in it. The images were collected at a nominal magnification of 60,000. Images were collected on a Philips CM12 thermionic emission electron microscope ( $C_s = 2.0$  mm, acceleration voltage = 120 kV), and on a Hitachi HF2000 field emission electron microscope ( $C_s = 2.6$  mm, acceleration voltage = 200 kV). All images in the data set contained about 2600 × 2600 pixels and the following parameters were used (see input box in Fig. 4): Amplitude contrast (*A*) = 7%, scanner pixel resolution (*DStep*) = 28.0 μm, pixel averaging (*Iave*) = 1, tile size (*Box*) = 128 pixels, resolution range (*ResMin*, *ResMax*) = 20–1.5 nm, defocus search range (*dFMin*, *dFMax*, and *FStep*) = 100–7000 nm in 100-nm steps. Accurate defocus values for these images are not known since the crystallographic methods for determining defocus values cannot be applied. The performance of the fitting procedure was therefore tested by varying the input parameters—amplitude contrast, tile size, and high-resolution limit. According to Table 2, the fitting procedure tends to give quite variable results when it fails. For example, when a tile size of 50 × 50 pixels was used, the changes in the defocus values in Table 2 were scattered between –8 and +4282 nm. We expect to see a similar pattern for the complex I images upon failure of the algorithm. Table 3 lists the average change, standard deviation, and the number of images deviating by more than 200 nm (indicated as fails), with respect to the initial fit using the parameters listed above. The table shows systematic changes in the defocus values when the value for the amplitude contrast is changed. These

Table 2  
Test of robustness of the CTFFIND3 algorithm when used on images that contain a carbon support film

Image	Amplitude contrast			Tile size				Resolution limit		
	0%	15%	35%	50	70	100	200	0.5 nm	1 nm	1.5 nm
b3730	·	·	$A_1 = -12$ $A_2 = -12$	$A_1 = 948$ $A_2 = 3821$	·	·	·	·	$A_x = 19$	$A_1 = 5282$ $A_2 = 154$
b3736	·	·	$A_1 = -10$ $A_2 = -12$	$A_1 = -8$ $A_2 = 4282$	·	·	·	·	$A_1 = -24$ $A_x = 9$	$A_1 = -474$ $A_2 = 470$
b3737	·	·	$A_1 = -12$ $A_2 = -13$	$A_1 = -26$ $A_2 = -149$	·	·	·	·	$A_2 = -40$	$A_1 = 579$ $A_2 = 3447$
b3739	·	·	$A_1 = -11$ $A_2 = -10$	$A_1 = -59$ $A_2 = 167$	·	·	·	·	$A_1 = 4227$ $A_2 = 2937$	$A_1 = -479$ $A_2 = 806$

The effect of changes in the input parameters—amplitude contrast, tile size, and high-resolution limit was tested. The changed parameters are indicated at the top of the table. Results from CTFFIND3 are compared with results listed in Table 1, where 7%, 128 × 128 pixels, and 0.3 nm were used for amplitude contrast, tile size, and high-resolution limit, respectively. Whenever the change in the measured defocus was smaller than 10 nm, and the change in stigmatic angle was smaller than 5°, a dot (·) is indicated. If the change for a parameter was larger than those limits, it is explicitly noted (units for the defocus changes are nanometer).

Table 3  
Test of robustness of the CTFFIND3 algorithm when used on images containing only protein embedded in ice

Average defocus	Amplitude contrast			Tile size				Resolution limit		
	0%	15%	35%	50	70	100	200	1.2 nm	1.8 nm	2.1 nm
1770-nm 104 images CM12	27 (4) 2 fails	-31 (5) 1 fail	-112 (15) 2 fails	-24 (43) 4 fails	-6 (41) 3 fails	-2 (24) 2 fails	-12 (27) 53 fails	-13 (40) 2 fails	37 (43) 3 fails	45 (49) 4 fails
4360-nm 20 images HF2000	42 (23) 0 fails	-43 (3) 0 fails	-154 (11) 0 fails	-38 (60) 1 fail	-9 (42) 1 fail	0 (36) 0 fails	-28 (33) 11 fails	-8 (25) 0 fails	10 (25) 1 fail	32 (72) 3 fails
6220-nm 144 images HF2000	42 (5) 1 fail	-49 (5) 0 fails	-176 (19) 0 fails	-64 (95) 64 fails	-12 (65) 7 fails	0 (41) 0 fails	-19 (30) 51 fails	-7 (36) 1 fail	10 (29) 1 fail	7 (38) 2 fails

The effect of changes in the input parameters—amplitude contrast, tile size, and high-resolution limit was tested. The changed parameters are indicated at the top of the table. Results from CTFFIND3 are compared with results obtained using 7%, 128 × 128 pixels, and 1.5 nm for amplitude contrast, tile size, and high-resolution limit, respectively. Whenever the change in defocus was larger than 200 nm, an image was counted as a “fail.” Otherwise, the average change in the measured defocus (in nanometer) and the standard deviation of changes (in nanometer, indicated in brackets) for a particular data set are listed.

changes have the same origin as those shown in Table 2 but they appear to be larger, presumably because the fit is now limited to lower resolution. This shows that it is important to enter a reasonably accurate value for the amplitude contrast. Table 3 suggests that the measured defocus decreases by about 5 nm when the amplitude contrast is increased by 1%. Nevertheless, the number of fails never exceeds 5% of all images in a data set and usually remains below 1%. The algorithm is more sensitive to the tile size and, for the images tested, it seems to work best with a tile size of approximately 100 × 100 pixels. Tile sizes of 50 × 50 and 200 × 200 pixels do not work well because of the limited sampling resolution and insufficient averaging, respectively. The algorithm is less sensitive with respect to changes in the high-resolution limit but fails more often when the resolution is limited to 2.1 nm, especially for the data set with the lowest defocus (1770 nm). As before, this is due to the fact that the first CTF zero for that data set is at about 2.4 nm, leaving few features in the observed power spectrum to be fitted. If the correct value for the amplitude contrast is known to within 10% and the other parameters are set within the range where the algorithm works most reliably, the average changes and standard deviations in Table 3 suggest that an accuracy of about 100 nm can be obtained. Using a similar argument as in Fig. 7, the resolution to which a correction of the CTF is reasonably accurate is about 0.8 nm, sufficient to correct data needed to visualize secondary structure in proteins. The working range of the parameters can easily be established for a data set by testing a few parameter combinations. Since a data set is usually collected at a particular defocus, the algorithm should determine the defocus parameters to be the same for most images, within an error of about 100 nm. This was the case for the complex I data sets used here.

To test the performance of the tilt estimation protocol, we used a series of images of 2D crystals of aquaporin (Murata et al., 2000), provided by Dr. Thomas

Walz. The crystals were applied to a continuous carbon film and embedded in trehalose. The images were recorded at a nominal magnification of 50,000, using the JEOL liquid helium field emission electron microscope JEM-3000SFF ( $C_s = 1.6$  mm, acceleration voltage = 300 kV). All images in the data set contained 10,000 × 15,000 pixels and the following parameters were used (see input box in Fig. 4): Amplitude contrast ( $A$ ) = 7%, scanner pixel resolution (DStep) = 7 μm, pixel averaging (Iave) = 2, tile size (Box) = 128 pixels, resolution range (ResMin and ResMax) = 20–0.7 nm, defocus search range (dFMin, dFMax, and FStep) = 50–3000 nm in 50-nm steps. Tilt parameters for these images had been previously obtained using EMTILT (Crowther et al., 1996) and were compared with the output of CTFTILT, as presented in Table 4. The values calculated using CTFTILT agree well with those obtained crystallographically: most tilt values agree within 1° or better, and most angles of the tilt axis agree within 2.5°. For one 60° image, image 660291, the tilt angle measured by CTFTILT was far from that obtained by EMTILT, suggesting a principle failure of the algorithm. The algorithm also failed on this image for all other combinations of input parameters tested (see below and Table 5). The algorithm failed when determining the defocus parameters in the center of the image, suggesting that the Thon rings for this image are weaker than in the other images. Inspection of the power spectrum calculated from the center of image 660291 confirmed that the Thon rings are weaker compared to the other 60° images analyzed. Furthermore, in the crystallographic analysis, image 660291 showed the smallest number of strong spots (spots with IQ values smaller than 4), confirming again that this image has weak contrast. For all other images tested, a maximum error in the local defocus values calculated from Eq. (9) can be calculated. If we assume a diameter of the exposed area of 1 μm, the error in the measured defocus near the edge of this area is smaller than 40 nm for all

Table 4  
Comparison of tilt parameters from aquaporin images

Image	Tilt axis $\phi$			Tilt angle $\gamma$			$CC_p$
	Crys.	CTFTILT	$\Delta\phi$	Crys.	CTFTILT	$\Delta\gamma$	CTFTILT
530394	93.8	96.4	2.6	19.6	20.7	1.1	0.19
530419	110.7	108.8	1.9	18.7	19.5	-0.8	0.19
530430	106.9	100.9	6.0	21.3	20.9	-0.4	0.19
530444	99.6	97.3	2.5	20.7	19.5	-1.2	0.18
660027	100.1	104.2	4.1	19.4	20.1	0.7	0.18
540149	94.6	87.5	7.1	43.1	44.0	0.9	0.18
540291	94.5	96.4	2.0	45.1	46.3	1.2	0.19
540302	93.5	92.1	1.4	44.7	43.1	-1.6	0.19
540313	95.8	96.1	0.3	44.0	44.4	0.4	0.18
660183	98.1	97.0	1.1	48.1	49.2	1.1	0.17
550089	92.6	92.7	0.1	60.5	61.2	0.7	0.17
660291	93.3	16.9	76.4	57.6	0.3	-57.3	0.17
660421	89.9	88.0	0.7	61.4	60.6	-0.8	0.17
680341	88.8	90.8	1.9	58.7	59.8	1.1	0.17

Tilt parameters from a refined aquaporin data set are compared with parameters derived from CTFTILT, with all measurements shown in degrees. The tilt axis angle is the angle from the tilt axis to the X-axis, and  $\Delta\phi$  and  $\Delta\gamma$  are the differences between each pair of measurements. The measurements agree well, except for image 660291 where the algorithm failed.

Table 5  
Test of robustness of the CTFTILT algorithm when used on images that contain a carbon support film

Image	Amplitude contrast			Tile size				Resolution limit		
	0%	15%	35%	50	70	100	200	0.5 nm	1 nm	1.5 nm
530394	.	.	.	.	.	.	.	.	.	$\Delta\gamma = 40$
530419	.	.	.	.	$\Delta\gamma = 41$	.	.	$\Delta\gamma = -18$	.	$\Delta\gamma = -16$
530430	.	.	.	$\Delta\gamma = 44$	.	.	.	.	.	$\Delta\gamma = -21$
530444	.	.	.	$\Delta\gamma = -15$	.	.	$\Delta\gamma = 22$	$\Delta\gamma = -20$	.	$\Delta\gamma = -17$
660027	.	.	.	$\Delta\gamma = 35$	$\Delta\gamma = 13$	.	.	.	.	$\Delta\gamma = -15$
540149	.	.	.	$\Delta\gamma = -10$	$\Delta\gamma = 17$	.	.	.	.	.
540291	.	.	.	$\Delta\gamma = 3.9$	$\Delta\gamma = 19$	.	.	.	.	$\Delta\gamma = -7.1$
540302	$\Delta\gamma = -17$	.	$\Delta\gamma = 29$	$\Delta\gamma = -28$	.	.	$\Delta\phi = 76$	.	.	$\Delta\gamma = -41$
540313	.	.	.	$\Delta\gamma = -44$	.	$\Delta\gamma = 21$	.	.	.	$\Delta\gamma = 9.0$
660183	.	.	.	$\Delta\gamma = 18$	.	.	$\Delta\gamma = -11$	.	.	$\Delta\gamma = -5.1$
550089	.	.	.	$\Delta\gamma = -61$	$\Delta\gamma = 3.5$	.	.	$\Delta\gamma = -60$	.	.
660291	$\Delta\gamma = -57$	$\Delta\gamma = -57$	$\Delta\gamma = -53$	$\Delta\gamma = -19$	$\Delta\gamma = -2.6$	$\Delta\gamma = -16$	$\Delta\gamma = -17$	$\Delta\gamma = 22$	$\Delta\gamma = -36$	$\Delta\gamma = -56$
660421	.	.	.	.	.	.	.	.	.	$\Delta\gamma = -4.4$
680341	.	.	.	.	.	$\Delta\gamma = -21$	$\Delta\gamma = -41$	.	.	.

The effect of changes in the input parameters amplitude contrast, tile size, and high-resolution limit was tested. The changed parameters are indicated at the top of the table. Results from CTFFIND3 are compared with results listed in Table 4, where 7%, 128 × 128 pixels, and 0.7 nm were used for amplitude contrast, tile size, and high-resolution limit, respectively. Whenever the changes in the measured tilt angle and tilt axis were smaller than 2°, a dot (·) is indicated. If the change for a parameter was larger than those limits, it is explicitly noted (units are in degrees).

images tested. The exceptions are images 660291 (algorithm failure) and 540149 where the large error in the tilt axis angle  $\phi$  (7.1°) produces a maximum error in the defocus values of about 70 nm.

As before, we tested the robustness of the algorithm by variation of the input parameters—amplitude contrast, tile size, and resolution limit. Table 5 summarizes the results. Whenever a change in an input parameter resulted in a change in the tilt angle or tilt axis direction larger than 2°, the error in the angle was written out in the table. For changes smaller than 2°, a dot (·) is shown, indicating no significant change. As shown in Table 5, changes in the value for the amplitude contrast do not change the result of the fit by much. However,

the algorithm is more sensitive to the choice of the tile size. In particular, a tile size of 50 × 50 or 70 × 70 pixels is too small due to the limited sampling resolution of the resulting power spectra. A tile size of about 100 × 100 pixels seems to work best. The resolution limit also affects the results, especially when it is set too low, thereby limiting the number of CTF zeros participating in the fit. Clearly, the CTFTILT algorithm is less robust than CTFFIND3. This is not surprising since apart from the defocus values, CTFTILT determines also the tilt angle and tilt axis. Furthermore, the algorithm often fails at the early stage when it tries to determine the defocus values in the center of the image. This is due to a more noisy power spectrum average that is calculated only

from the central area of the image covered by the 11 parallel lines (Fig. 5). According to Table 5, the average rate of failure of CTFTILT lies between 7 and 21%.

As a final test of CTFTILT, the tilt angle and tilt axis direction were determined for the 268 images of single mitochondrial complex I. Although all of these images were collected without introducing a deliberate tilt, small local tilts in a specimen are unavoidable due to undulations of the carbon film and small bents in the copper support grid (Vonck, 2000). The same input parameters were used when these images were used to test CTFFIND3: Amplitude contrast ( $A$ ) = 7%, scanner pixel resolution (DStep) = 28.0  $\mu\text{m}$ , pixel averaging (Iave) = 1, tile size (Box) = 128 pixels, resolution range (ResMin and ResMax) = 20–1.5 nm, defocus search range (dFMin, dFMax, and FStep) = 100–7000 nm in 100-nm steps. Table 6 lists the average change in the tilt angle, standard deviation, and the number of images deviating by more than  $10^\circ$  (fails), with respect to the tilt angles from the initial fit using the parameters listed above. The average change in the tilt angle is usually smaller than  $1^\circ$  and never exceeds  $2.2^\circ$ . The standard deviation of the tilt angle change is about  $4^\circ$ , and there are about 10% of images with a measured tilt angle deviating by more than  $10^\circ$  from the initial fit (fails). In some cases, the standard deviation and fail rate are higher, for example when a tile size of  $50 \times 50$  pixels is used, or if the high-resolution limit is set to 2.1 nm. Those settings were also found in the previous test to produce less reliable results (see Table 3). The average changes and standard deviations listed in Table 6 suggest that the tilt angle of a specimen lacking a carbon film can be determined with an accuracy of about  $6^\circ$ . The changes in the measured tilt axis direction are not listed in Table 6 since the tilt axis is rather poorly defined in images of samples with a small tilt. Typically,

the standard deviation for the measured tilt axis direction was about  $30^\circ$ . It is interesting to note that the standard deviation of tilt angles from zero, determined for all three sets of images was about  $10^\circ$ , twice the standard deviation observed for the reproducibility of measurements of the algorithm. This suggests that many images were recorded from samples with significant local tilts even though the nominal tilt adjusted on the microscope was zero.

#### 4. Discussion

Precise defocus and tilt information is essential for high-resolution protein structure analysis using electron microscopy. The oscillations visible in the power spectrum of an electron micrograph (Thon rings; Thon, 1966) have been used before to determine defocus parameters for untilted specimens (for example, Conway and Steven, 1999; Frank, 1972; Henderson et al., 1986; Ludtke et al., 1999; Morgan et al., 1995; Tani et al., 1996; Zhu et al., 1997), and to obtain tilt information (Henderson and Unwin, 1975; van Heel et al., 2000). Existing procedures require a varying degree of user interaction. The computer programs CTFFIND3 and CTFTILT run in a fully automated fashion and can be used to process hundreds of images in a relatively short time. Since they do not rely on crystallographic methods for the determination of defocus and tilt parameters, they can be used on images containing any type of sample. The only required set-up consists of finding a set of input parameters that yield reliable defocus and tilt measurements for a particular set of images. Once these parameters are approximately known, they can be used for all images in an entire data set without readjustment, yielding a relatively low rate of algorithm failure (see below).

Table 6

Test of robustness of the CTFTILT algorithm when used on images containing only protein embedded in ice

Average defocus	Amplitude contrast			Tile size				Resolution limit		
	0%	15%	35%	50	70	100	200	1.2 nm	1.8 nm	2.1 nm
1772-nm 104 images CM12	-0.2 (1.1) 0 fails	0.3 (2.0) 4 fails	0.2 (3.4) 12 fails	0.5 (3.9) 36 fails	-0.1 (2.7) 4 fails	0 (1.9) 3 fails	0.3 (2.0) 2 fails	0.3 (3.6) 0 fails	0.5 (4.0) 1 fail	0.1 (3.3) 4 fails
4364-nm 20 images HF2000	0.2 (0.7) 0 fails	0 (0.7) 0 fails	0.7 (2.3) 1 fail	-0.6 (5.5) 14 fails	-1.2 (3.7) 2 fails	-1.4 (2.5) 0 fails	-0.4 (2.4) 1 fail	-0.9 (3.8) 1 fail	-2.2 (5.4) 0 fails	0.2 (3.6) 3 fails
6216-nm 144 images HF2000	0 (1.3) 1 fail	0.1 (1.3) 0 fails	-0.2 (3.0) 8 fails	1.4 (5.5) 103 fails	1.4 (4.4) 4 fails	-0.6 (3.9) 14 fails	0.3 (3.2) 9 fails	0.4 (3.7) 11 fails	0.1 (3.5) 17 fails	-0.1 (4.6) 20 fails

The effect of changes in the input parameters—amplitude contrast, tile size, and high-resolution limit was tested. The changed parameters are indicated at the top of the table. Results from CTFTILT are compared with results obtained using 7%,  $128 \times 128$  pixels, and 1.5 nm for amplitude contrast, tile size, and high-resolution limit, respectively. Whenever the change in the measured tilt angle was larger than  $10^\circ$ , an image was counted as a “fail.” Otherwise, the average change in the measured tilt angle (in degrees) and the standard deviation of changes (in degrees, indicated in brackets) for a particular data set are listed.

The present study attempts to use defocus and tilt information obtained crystallographically from a number of images of 2D crystals to estimate the accuracy that can be obtained for these parameters by fitting Thon ring oscillations. Such an evaluation was done previously using a single image of an untilted 3D microcrystal of calcium ATPase, suggesting that an accuracy of about 10 nm can be obtained (Tani et al., 1996). The crystal images we employed here were used to calculate a high-resolution projection map of bacteriorhodopsin (Grigorieff et al., 1995) and a high-resolution map of aquaporin (Murata et al., 2000). The high resolution implies that the defocus, astigmatism, tilt angle, and tilt axis were known accurately for these images. The comparison of results from our new computer program CTFFIND3 with those obtained crystallographically (Table 1) suggest that our Thon ring analysis gives defocus values with an error smaller than 10 nm, sufficient for reliable measurement of phases in an untilted image out to 0.3-nm resolution. Thus, the attainable accuracy is similar to that found by Tani et al. (1996). The error of the determined defocus values is probably even smaller than suggested by the comparison with the crystallographic data as any errors in the latter are unknown and, therefore, were ignored in this analysis. There are, however, a number of sources of error associated with our approach. First, a systematic error may be introduced by the carbon support film that contributes part of the contrast in the images of the 2D crystals. Since the carbon film is not in the same plane as the crystals, its associated image defocus will differ slightly from that of the crystals. Second, if the amount of amplitude contrast in an image is not known accurately, systematic shifts in the measured defocus values could be introduced (see Table 2). Third, for larger defocus values, the envelope function may limit the visibility of the Thon rings at higher resolution, and this could lead to a less accurate fit.

The accuracy of the determined defocus values is generally lower for images of single protein particles where the contrast originates solely from ice and the embedded protein. As the tests reported in Table 3 suggest, errors in the defocus values are about 10 times larger than those observed for the images of the 2D bacteriorhodopsin crystals, due to the weaker contrast in the images. In addition, the systematic shift introduced by an inaccurate value for the amplitude contrast is larger than in the crystal images. This is likely due to the smaller number of Thon rings in the single particle images that are visible mainly at low resolution. At low resolution, a small shift in the position of a CTF zero introduced by an inaccurate value for the amplitude contrast would have to be compensated for by the fitting procedure with a larger change in the defocus value than at higher resolution. Finally, the measured average defocus of an image of ice-embedded single protein par-

ticles will deviate from the true defocus of individual particles because the particles will, in general, assume different depths in the ice (for example, see van Heel et al., 2000; Zhu et al., 1997).

For tilted specimens, the errors in tilt angle and tilt axis given in Table 4 are again upper limits as errors in the crystallographic values obtained using the computer program EMTILT (Crowther et al., 1996) are not known and were not taken into account. Table 4 suggests that our new computer program CTFTILT can determine the tilt angle to within  $1^\circ$ , and the tilt axis to within  $2.5^\circ$ . The determined values for tilt angle and axis serve, therefore, as good starting values for images of 2D crystals to merge a data set and calculate a preliminary 3D structure that can be used for subsequent parameter refinement using crystallographic methods. When images of untilted and slightly tilted specimens are analyzed that do not contain contrast from a carbon support film, the error in the tilt angle measurement is higher, about  $6^\circ$  (see Table 6).

The algorithms in CTFFIND3 and CTFTILT fail occasionally, as shown in Tables 2, 3, 5, and 6. The analysis of untilted images containing carbon film (Table 2) is the most robust and failures were only detected for certain combinations of input parameters when the algorithm failed in 100% of the images tested. When no carbon film is present, CTFFIND3 fails at a rate of about 5% or less (Table 3). The CTFTILT algorithm has a higher failure rate (between 7 and 21%, see Table 5) for two reasons: First, it must determine a larger number of parameters, and second, it uses a noisier average power spectrum to determine initial defocus values in the center of the image. Not only is this power spectrum average derived from a smaller area of the image compared with the entire image used in CTFFIND3, but the defocus is also variable across this small area. This defocus variability will attenuate the Thon rings in a direction of the average power spectrum perpendicular to the tilt axis, making it more difficult to achieve a good fit. Consequently, the rate of failure of CTFTILT is highest for the images of the  $60^\circ$  tilted specimens (Table 5). Finally, the images of the tilted 2D crystals tested in Tables 4 and 5 were recorded at 300 kV. Compared to images recorded at 200 kV and lower, the contrast in these images is weakened (Miyazawa et al., 1999), making the fitting of the Thon rings again more difficult. The rate of failure is about 10% (Table 6) when used on images of specimens with small or no tilt that do not contain contrast from a carbon film. Failure of the algorithm usually produces defocus values and tilt angles that differ substantially from values obtained for other images in the same data set (see Tables 2 and 5), making those cases easy to detect. In some cases, however, the failure consists of smaller deviations from the correct values. If a failure of the algorithm remains undetected for a small part of the images, correction for the CTF

based on the incorrectly determined defocus or tilt values will produce erroneous phases. These are detectable at a later stage in the processing of these images by comparing the data with an average based on the entire data set.

## 5. Conclusions

We have developed two computer programs, CTF-FIND3 and CTFTILT, that determine defocus and astigmatism in images of untilted specimens, and defocus, astigmatism tilt angle, and tilt axis direction in images of tilted specimens, respectively. The programs run fully automatically and can determine defocus and tilt parameters with high accuracy. The accuracy of the algorithms were tested on untilted and tilted images of two-dimensional crystals with known defocus and tilt values, and on images of untilted and slightly tilted specimens of single protein complexes. The robustness of the algorithms was evaluated using a number of different input control parameters. The universal applicability of the algorithms will simplify current procedures for the processing of images of biological specimens to high resolution when correction of the contrast transfer function is required.

## Acknowledgments

The authors thank Dr. Thomas Walz for providing images of aquaporin crystals to test our algorithms. The authors are grateful to Dr. David DeRosier, Dr. Thomas Walz, and Dr. Brian Andrews for critical comments on the manuscript. This work was supported in part by NIH Grants GM-62580 (N.G.) and DK-2801 (J.M.).

## References

- Böttcher, B., Wynne, S.A., Crowther, R.A., 1997. Determination of the fold of the core protein of hepatitis B virus by electron cryomicroscopy. *Nature* 386, 88–91.
- Conway, J.F., Steven, A.C., 1999. Methods for reconstructing density maps of “single” particles from cryoelectron micrographs to subnanometer resolution. *J. Struct. Biol.* 128, 106–118.
- Erickson, H.P., Klug, A., 1971. Measurement and compensation of defocusing and aberrations by Fourier processing of electron micrographs. *Phil. Trans. R. Soc. Lond. Ser. B* 261, 105.
- Fernandez, J.J., Sanjurjo, J.R., Carazo, J.M., 1997. A spectral estimation approach to contrast transfer function detection in electron microscopy. *Ultramicroscopy* 68, 267–295.
- Frank, J., 1972. Study on heavy/light atom discrimination in bright-field electron-microscopy using computer. *Biophys. J.* 12, 484.
- Frank, J., Agrawal, R.K., 2000. A ratchet-like inter-subunit reorganization of the ribosome during translocation. *Nature* 406, 318–322.
- Grigorieff, N., 1998. Three-dimensional structure of bovine NADH:ubiquinone oxidoreductase (complex I) at 22 Å in ice. *J. Mol. Biol.* 277, 1033–1046.
- Grigorieff, N., Beckmann, E., Zemlin, F., 1995. Lipid location in deoxycholate-treated purple membrane at 2.6 Å. *J. Mol. Biol.* 254, 404–415.
- Henderson, R., Baldwin, J.M., Ceska, T.A., Zemlin, F., Beckmann, E., Downing, K.H., 1990. An atomic model for the structure of bacteriorhodopsin. *Biochem. Soc. Trans.* 18, 844.
- Henderson, R., Baldwin, J.M., Downing, K.H., Lepault, J., Zemlin, F., 1986. Structure of purple membrane from halobacterium—halobium—recording, measurement and evaluation of electron-micrographs at 3.5 Å resolution. *Ultramicroscopy* 19, 147–178.
- Henderson, R., Unwin, P.N., 1975. Three-dimensional model of purple membrane obtained by electron microscopy. *Nature* 257, 28–32.
- Koeck, P.J., 2000. Ins and outs of digital electron microscopy. *Microsc. Res. Tech.* 49, 217–223.
- Kühlbrandt, W., Wang, D.N., 1991. Three-dimensional structure of plant light-harvesting complex determined by electron crystallography. *Nature* 350, 130–134.
- Kuhn, R.J., Zhang, W., Rossmann, M.G., Pletnev, S.V., Corver, J., Lenches, E., Jones, C.T., Mukhopadhyay, S., Chipman, P.R., Strauss, E.G., Baker, T.S., Strauss, J.H., 2002. Structure of dengue virus: implications for flavivirus organization, maturation, and fusion. *Cell* 108, 717–725.
- Mindell, J.A., Maduke, M., Miller, C., Grigorieff, N., 2001. Projection structure of a CIC-type chloride channel at 6.5 Å resolution. *Nature* 409, 219–223.
- Miyazawa, A., Fujiyoshi, Y., Stowell, M., Unwin, N., 1999. Nicotinic acetylcholine receptor at 4.6 Å resolution: transverse tunnels in the channel wall. *J. Mol. Biol.* 288, 765–786.
- Morgan, D.G., Owen, C., Melanson, L.A., DeRosier, D.J., 1995. Structure of bacterial flagellar filaments at 11 Å resolution: packing of the  $\alpha$ -helices. *J. Mol. Biol.* 249, 88–110.
- Murata, K., Mitsuoka, K., Hirai, T., Walz, T., Agre, P., Heymann, J.B., Engel, A., Fujiyoshi, Y., 2000. Structural determinants of water permeation through aquaporin-1. *Nature* 407, 599–605.
- Nogales, E., Wolf, S.G., Downing, K.H., 1998. Structure of the  $\alpha\beta$  tubulin dimer by electron crystallography. *Nature* 391, 199–203.
- Ramachandran, G.N., Srinivasan, R., 1961. An apparent paradox in crystal structure analysis. *Nature* 190, 159–161.
- Ranson, N.A., Farr, G.W., Roseman, A.M., Gowen, B., Fenton, W.A., Horwich, A.L., Saibil, H.R., 2001. ATP-bound states of GroEL captured by cryo-electron microscopy. *Cell* 107, 869–879.
- Smith, M.F., Langmore, J.P., 1992. Quantitation of molecular densities by cryoelectron microscopy—determination of the radial density distribution of tobacco mosaic-virus. *J. Mol. Biol.* 226, 763–774.
- Tani, K., Sasabe, H., Toyoshima, C., 1996. A set of computer programs for determining defocus and astigmatism in electron images. *Ultramicroscopy* 65, 31–44.
- Thon, F., 1966. Zur Defokussierungsabhängigkeit des Phasenkontrastes bei der elektronenmikroskopischen Abbildung. *Z. Naturforsch.* 21a, 476–478.
- Toyoshima, C., Unwin, N., 1988. Contrast transfer for frozen-hydrated specimens: determination from pairs of defocused images. *Ultramicroscopy* 25, 279–291.
- Toyoshima, C., Yonekura, K., Sasabe, H., 1993. Contrast transfer for frozen-hydrated specimens. 2. Amplitude contrast at very low-frequencies. *Ultramicroscopy* 48, 165–176.
- van Heel, M., Gowen, B., Matadeen, R., Orlova, E.V., Finn, R., Pape, T., Cohen, D., Stark, H., Schmidt, R., Schatz, M., Patwardhan, A., 2000. Single-particle electron cryo-microscopy: towards atomic resolution. *Quart. Rev. Biophys.* 33, 307–369.
- Vonck, J., 2000. Parameters affecting specimen flatness of two-dimensional crystals for electron crystallography. *Ultramicroscopy* 85, 123–129.
- Wade, R.H., 1992. A brief look at imaging and contrast transfer. *Ultramicroscopy* 46, 145–156.

- Wells, A.L., Lin, A.W., Chen, L.Q., Safer, D., Cain, S.M., Hasson, T., Carragher, B.O., Milligan, R.A., Sweeney, H.L., 1999. Myosin VI is an actin-based motor that moves backwards. *Nature* 401, 505–508.
- Wendt, T.G., Volkman, N., Skiniotis, G., Goldie, K.N., Muller, J., Mandelkow, E., Hoenger, A., 2002. Microscopic evidence for a minus-end-directed power stroke in the kinesin motor *ncd*. *EMBO J.* 21, 5969–5978.
- Zemlin, F., Beckmann, E., vanderMast, K.D., 1996. A 200 kV electron microscope with Schottky field emitter and a helium-cooled superconducting objective lens. *Ultramicroscopy* 63, 227–238.
- Zhou, Z.H., Baker, M.L., Jiang, W., Dougherty, M., Jakana, J., Dong, G., Lu, G., Chiu, W., 2001. Electron cryomicroscopy and bioinformatics suggest protein fold models for rice dwarf virus. *Nat. Struct. Biol.* 8, 868–873.
- Zhou, Z.H., Chiu, W., 1993. Prospects for using an Ivern with a Feg for imaging macromolecules towards atomic resolution. *Ultramicroscopy* 49, 407–416.
- Zhu, J., Frank, J., 1994. Accurate retrieval of transfer function from defocus series. In: *Proceedings of the 13th International Congress on Electron Microscopy*, Paris, France.
- Zhu, J., Penczek, P.A., Schroder, R., Frank, J., 1997. Three-dimensional reconstruction with contrast transfer function correction from energy-filtered cryoelectron micrographs: procedure and application to the 70S *Escherichia coli* ribosome. *J. Struct. Biol.* 118, 197–219.